Article

Characterization of the Plasma Generated by a Compact Theta Pinch

Sagi Turiel *, Alexander Gribov, Daniel Maler ⬤ and Yakov E. Krasik *⬤

Physics Department, Technion, Israeli Institute of Technology, Haifa 3200003, Israel; daniel@nt-tao.com (D.M.)
* Correspondence: sagie.turiel@campus.technion.ac.il (S.T.); fnkrasik@physics.technion.ac.il (Y.E.K.)

Abstract: Theta Pinch is one of the promising methods for the generation of hot and dense plasma. In this paper, we describe the results of experimental research on a small-scale Theta Pinch created with Helium or Hydrogen plasmas. Different plasma diagnostics, namely, optical, microwave cut-off, laser interferometry, visible spectroscopy, Thomson scattering, and Laser-Induced Fluorescence were used to characterize the time- and space-resolved evolution of the plasma parameters, and the specific features of these diagnostic results obtained are discussed. The measured plasma density and the electron and ion temperature evolution, obtained by these various diagnostic tools, agree to a satisfactory level. These methods will be applied for studies of the parameters of the plasma in the device that is being developed by the nT-Tao company towards fusion energy.

1. Introduction

One of the first methods used in the attempts towards achieving inertial confinement fusion was the Theta Pinch (TP), introduced more than 70 years ago [1]. Since its conceptualization, many theoretical, numerical simulations and experimental studies were carried out to characterize the temporal and spatial behavior of the plasma in this device [1–20]. In the TP configuration, the plasma is generated by the ionization of a gas inside a dielectric tube, the result of an azimuthal voltage induced by a fast-rising high current in an external coil supplied by a pulse power generator. This induced voltage accelerates background free electrons in the gas to an energy sufficient for the impact ionization of gas atoms or molecules. An avalanche is initiated, leading to the formation of a highly ionized plasma sheath in the vicinity of the internal tube surface, where the induced voltage obtains maximal value. A current is induced in the plasma sheath, carried by the electrons, generating a self-magnetic azimuthal field. The interaction of this field with the magnetic field of the current flowing in the coil leads to a significant magnetic field gradient (magnetic pressure) acting as a piston on the current-carrying plasma sheath. This piston creates a shock, propagating inwards toward the axis, while the gas is ionized behind its front. The main plasma sheath's radial propagation is accompanied by increasing density and temperature, which reach their maximal values in the vicinity of the axis. Earlier research demonstrated that a large electron density plasma, with values exceeding 10^{16} cm^{-3} and a few hundred eV-temperature, forms due to this implosion process [2].

The most common model describing the TP, so far the best, was introduced by Lee [8,16]. This model assumes that a plasma sheath acts as a compressing piston, generating an imploding shockwave that sweeps and ionizes the gas behind its front, a process known as the snow-plow model. The set ordinary differential equations (ODEs) derived by Lee calculate the shockwave and plasma sheath compression with quite good accuracy accounting for the parameters of the electrical circuit, gas type, and the geometry of the TP. There are two fitting parameters in these equations. The first parameter f is related to the coupling between the circuit and the plasma current while the second parameter f_m

describes the fraction of mass being swept by the shock. The time evolution of the loop current and piston and shock front radii are obtained by solving the following ODEs [16]:

$$\frac{dI}{dt} = \frac{V_0 - \frac{1}{C_0}\int I\,dt - R_0 I + 2f\frac{\pi\mu_0}{l_c}r_p I\frac{dr_p}{dt}}{L_0 + \frac{\pi\mu_0}{l_c}\left(r_c^2 - fr_p^2\right)}, \tag{1}$$

$$\frac{dr_p}{dt} = \frac{\frac{2\gamma}{\gamma+1}\frac{r_s}{r_p}\frac{dr_s}{dt} - \frac{r_p}{I}\left(1 - \frac{r_s^2}{r_p^2}\right)\frac{dI}{dt}}{\gamma - 1 + \frac{r_s^2}{r_p^2}}, \tag{2}$$

$$\frac{dr_s}{dt} = -\sqrt{\frac{\mu_0(\gamma+1)}{4}\frac{f(2-f)}{f_m}\frac{1}{l_c^2\rho_0}I}, \tag{3}$$

where V_0 is the charging voltage of the pulse power supply based on capacitive storage and C_0, R_0, and L_0 are the capacitance, resistance, and inductance of the electrical circuit, respectively. I is the discharge current, μ_0 is the vacuum permeability, and l_c and r_c are the coil width and radius, respectively. r_p and r_s are the piston and shockwave radii, respectively; $\gamma \approx 1.67$ is the specific heat ratio assuming a fully ionized Hydrogen plasma [21]; ρ_0 is the gas initial density; and f and f_m are the fitting parameters.

Non-perturbing diagnostics of the plasma generated in the TP, measuring its parameters, are crucial. We present the results of experimental studies of plasma generated by a compact Theta Pinch that was designed and assembled in the Plasma Physics and Pulsed Power Laboratory at the Technion. To characterize the TP, several non-perturbing, temporally and spatially resolved, diagnostic methods were employed. These include electrical current and voltage monitors, optical imaging, microwave cut-off, laser interferometry, visible spectroscopy, Thomson scattering, and Laser-Induced Fluorescence (LIF), which were applied for the characterization of the plasma dynamic parameters. The main purpose of this study is to explore the applicability of these various, non-perturbing diagnostic methods that will be applied in a much more powerful plasma device being developed at nT-Tao [22].

2. Experimental Setup and General Parameters of the Theta Pinch

The experimental setup, sketched in Figure 1, consists of a 65 mm inner diameter Pyrex tube, an induction coil for plasma production, and a pulsed power supply. An initial vacuum in the tube of 1 mPa was produced by a turbopump (MacroTorr turbo-V 250, Torino, Italy) and scroll pump (EDWARDS nXDS15i, Opava, Czech Repoblic). The tube was filled with either Hydrogen or Helium gas at a pressure range of 10–1330 Pa using precise vents and controlled by a baratron gauge (Edwards model 655 AB, Wilmington, MA, USA). A total of 99.99% pure Helium gas was supplied by a gas cylinder. An MRC GG-H-200 generator (MCR Laboratory Equipment, Holon, Israel) was used to produce Hydrogen. Continuous pumping and gas injection, keeping constant pressure and using precise gas vents, ensures gas purity in the tube.

For reliable plasma discharge ignition, a sharp cone tungsten electrode was installed in the tube. The electrode is biased to −2 kV pre-ionization voltage supplied by a DC high-voltage unit (VC 952 A, Tennelec, Meriden, CT, USA) via a 2 MΩ resistor connected in series with the electrode. This voltage was sufficient to produce a corona-like discharge, which supplies free electrons to the gas filling the tube volume.

Characterization of the plasma using microwave cut-off and laser interferometry was carried out with a three-loop coil 0.5 mm thick, 20 mm-wide copper foil, coil arrangement wrapped around the glass tube. The advantage of a three-loop coil is that given an equal dI/dt of the discharge current, a larger magnetic field flux, Φ_3, is generated compared to the magnetic field flux, Φ_1, generated by a single loop. Thus, the three-loop coil generates a larger induced voltage, ε_3, than that induced by a single-loop coil, ε_1, as seen here:

$\varepsilon_3/\varepsilon_1 = 3(L_g + L_1)/(L_g + 3L_1)$, where L_g and L_1 are the inductances of the pulse generator and a single coil, respectively.
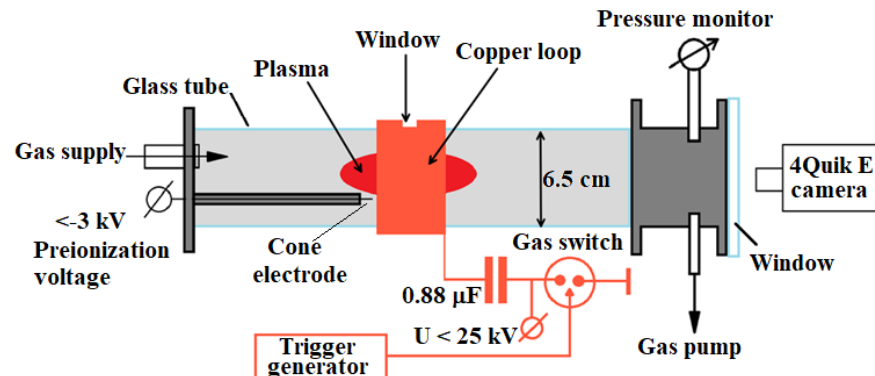

Figure 1. The experimental setup used to produce a Theta Pinch with a single loop.

Although a three-loop coil can produce a larger induced voltage (when the condition $L_g \gg L_1$ is satisfied), the plasma forms with spatial non-uniformities across the tube due to the discrete number of turns having, in the present setup, gaps of ~2 cm. Therefore, in experiments involving fast framing imaging of the plasma light emission, spectroscopy, Thomson scattering, and LIF, we used a setup with only a single turn of 0.5 mm thick and 40 mm-wide copper foil.

Two pulse-power, high-current generators were applied in this research for the generation of TP plasma. A Fluke 40 kV DC voltage divider, was used to control the charging voltage of the generators, and a Pierson current monitor (model 5046, Palo Alto, CA, USA) was used to measure the discharge current, the waveform of which was registered by a Tektronix TDS-784A (Beaverton, OG, USA) (1 GHz, 4 Gs/s) oscilloscope. The generator used for the three-loop coil setup consisted of a low-inductance 1 μF, 20 kV capacitor (Condenser Products Corp., Brooksville, FL, USA) charged to 17 kV (stored energy of ~145 J) and discharged using a gas spark gap switch with an externally triggered middle distortion electrode. A typical waveform of the discharge current obtained at a He gas pressure of 0.1 Pa when a plasma discharge did not develop is shown in Figure 2. The discharge current is characterized by ~1.5 μs rise time, reaching an amplitude of I = 17.5 kA and $dI/dt \approx 1.1 \times 10^{10}$ A/s. However, due to an underdamped discharge, characterized by current oscillations with a ~34.8 μs decay, the lifetime of this capacitor was limited to several hundreds of shots. A second generator, based on two 0.44 μF, 50 kV, 20 nF capacitors (General Atomics, San Diego, CA, USA) connected in parallel, operated at 25 kV charging voltage (stored energy of 275 J), which is smaller than its nominal value by a factor of two. This generator was used in experiments with a single-loop coil (see Figure 1). For this case, a 0.7 μs rise time, ~29 kA amplitude discharge current (see Figure 2) with $dI/dt \approx 4.1 \times 10^{10}$ A/s was obtained with a fast ~7 μs decay time (see Figure 2). Matching the results of an underdamped RLC circuit current oscillation, shown in Figure 2, allows us to calculate the inductance L_0 and the resistance R_0 from the measured oscillation frequency $f = (2\pi)^{-1}\sqrt{(1/L_0 C_0) - (L_0/2R_0)^2}$ and the current decay coefficient $\tau = L/2R$. Here, C_0 is the capacitance of the storage capacitor. Let us note that, shown in Figure 2, current waveforms were measured with no plasma generation; thus, no plasma effects were present. These values of L_0, C_0, and R_0 were used while simulating Equations (1)–(3). We calculated the impedance, inductance, and resistance of the three-loop and single-loop setups as ~0.93 Ω, ~0.95 μH, and ~17 mΩ and ~0.7 Ω, ~0.56 μH, and ~14 m Ω, respectively.

As a result of the fast discharge, a longitudinal oscillating magnetic field is generated in the tube, which, in turn, induces an azimuthal electric field. We estimated the electric field in the vicinity of the loop as $\left|\vec{E}\right| = \frac{L}{2\pi r_0}\frac{dI}{dt}$, where $L \approx N\mu_0 r_0\left[\ln\left(\frac{8l}{r_0+l}\right) - 0.5\right]$ is the inductance of a coil with N loops of $r_0 = 3.25$ cm (loop radius) and $l = 2$ cm foil

width. These estimates give $\left|\overrightarrow{E}_3\right|$ ~40.5 V/cm and $\left|\overrightarrow{E}_1\right|$ ~50.4 V/cm for the three-loop and single-loop setups, respectively. These electric fields accelerate free electrons, which acquire sufficient energy for gas ionization, resulting in an avalanche and a current-carrying plasma sheath. The interaction of the induced magnetic field created by the plasma current with the external magnetic field of the current in the coil leads to a magnetic field gradient, which compresses the plasma. Thus, the energy of the time-dependent magnetic field, created by the current flowing in the loop, is transferred into ionization and excitation of the gas and radial compression of the plasma sheath.
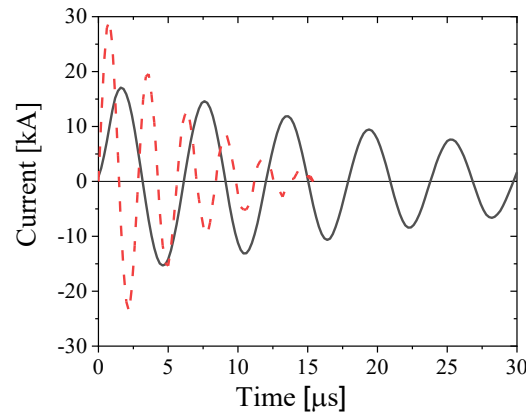
Figure 2. Waveforms of the current for the 1 μF capacitor charged to 17 kV and discharged into the three-loop coil (black line) and two 0.44 μF capacitors connected in parallel, charged to 25 kV and discharged into a single-loop coil (red dashed line). The He gas pressure in the tube was 0.1 Pa.

In Figure 3a, we present waveforms of the discharge current in a three-loop coil obtained with He gas at P = 2.7 kPa and at P = 0.4 kPa. For the higher pressure, plasma formation was not obtained. When plasma forms, a much faster decay of the discharge current is observed due to energy transfer to the gas ionization and plasma compression. In Figure 3b, we present dependencies of the energy transfer to Helium and Hydrogen plasmas as functions of pressure.
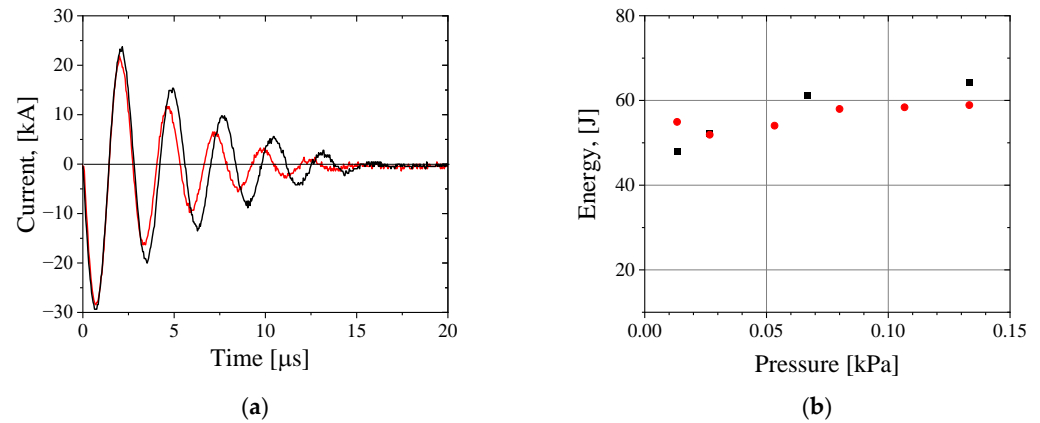

(**a**)

(**b**)
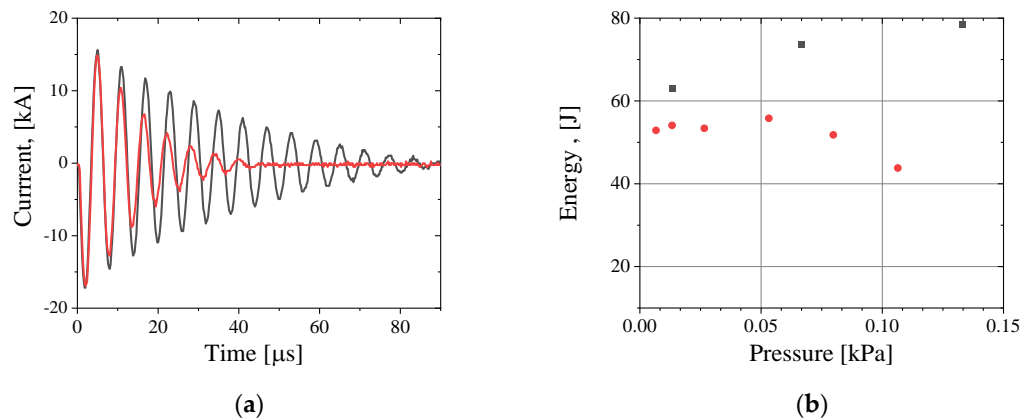
Figure 3. Three-loop Theta Pinch coil. (**a**) Waveforms of the discharge current at 2.7 kPa pressure when no plasma generation was obtained (black) and with the plasma generation at 0.4 kPa (red) pressure of He gas. (**b**) Energy deposited into the gas discharge vs. gas pressure for He (black squares) and H_2 (red dots).

For He plasma, up to 55% of the stored energy was transferred to the plasma, while for Hydrogen plasma, it was $\leq$ 38%. Here, the energy transferred to the plasma was calculated as the time-integrated power, $P_{loop} = \int_0^t I^2 R dt$, subtracted from the total energy initially

stored in the capacitor. The resistance R was calculated using the decay constant τ of the discharge current $R = L/2\tau$.

In Figure 4a, we present waveforms like those shown in Figure 3 but obtained with a single loop at 0.1 Pa and 0.4 kPa of He gas pressure. As in the three-loop scheme, when plasma generation occurs, current oscillations decay faster. Figure 4b presents the stored energy transfer to the plasma for different gas pressures. The efficiency of the energy transfer to the plasma is smaller than those obtained for the three-loop scheme. This can be explained by the smaller period of the current oscillations, meaning that the time for energy transfer to the plasma during its compression was not sufficient.

(a)

(b)

Figure 4. Single-loop Theta Pinch. (**a**) Waveforms of the discharge current obtained in the case of Helium gas at 0.1 Pa pressure when no plasma generation was obtained (black) and with plasma generation at 0.4 kPa (red) pressure of He gas. (**b**) Energy deposited into the gas discharge versus He (black squares) and H_2 (red dots) pressure.

3. Experimental Results

3.1. Time and Space-Resolved Light Emission During Plasma Compression

In Figure 5, we show an example of Hydrogen plasma light emission images obtained using a 4QuikE intensified camera (Stanford Computer Optics, Berkeley, CA, USA) during plasma compression at P = 63 Pa. In experiments with a single loop, the 4QuikE camera was installed in front of the glass tube along its axis, with its focus set on the center of the loop (see Figure 1). The images presented in the upper row of Figure 5 reveal that the bright light emission from the plasma is obtained at the periphery of the tube, approximately half a period after the beginning of the discharge current, and plasma compression takes ~1 μs. This time is estimated when the spatial size of the plasma emission pattern reaches its smallest value (~5 mm). The latter allows us to estimate the average implosion velocity of the plasma as $\sim 3 \cdot 10^6$ cm/s at 63 Pa gas pressure for both Hydrogen and Helium. Side view images obtained for the three-loop coil setup (see the images in the bottom row of Figure 5) show non-uniform plasma formation along the width of the loops. Additionally, the plasma is compressed to a larger final radius compared to the single-loop experiments.

We used a fast photodiode (DET02AFC, Thorlabs, Newton, NJ. USA) to obtain the time evolution of the light emission from the plasma. In the photodiode data (see Figure 6), compression is seen as the fast-rising intensity and the quality of compression can be estimated by the duration and amplitude of the first peak in the light intensity. A light emission from the plasma was obtained over 80 μs, giving an estimated plasma lifetime.

In Figure 7, we present the results of numerical simulations using the Lee model for the three-loop and single-loop setups. Here, one can see a compression of the plasma to its minimal radius at the time when the plasma is compressed for the first time. In the single-loop scheme, this occurs at ~5 μs after the beginning of the current, whereas in the three-loop scheme, it occurs at ~3 μs. The simulated current waveform shows satisfactory agreement with the measured current for fitting parameter values of $f = f_m = 0.9$. Numerically calculated shock and piston radii show maximum implosion velocities of ~1.5×10^7 cm/s

and $\sim 4.8 \times 10^6$ cm/s, respectively, for a single loop. This result agrees satisfactorily with the average velocity of the plasma implosion obtained using the framing images of the plasma light intensity. For the three-loop setup, these velocities are $\sim 5 \times 10^6$ cm/s and $\sim 1.5 \times 10^6$ cm/s.
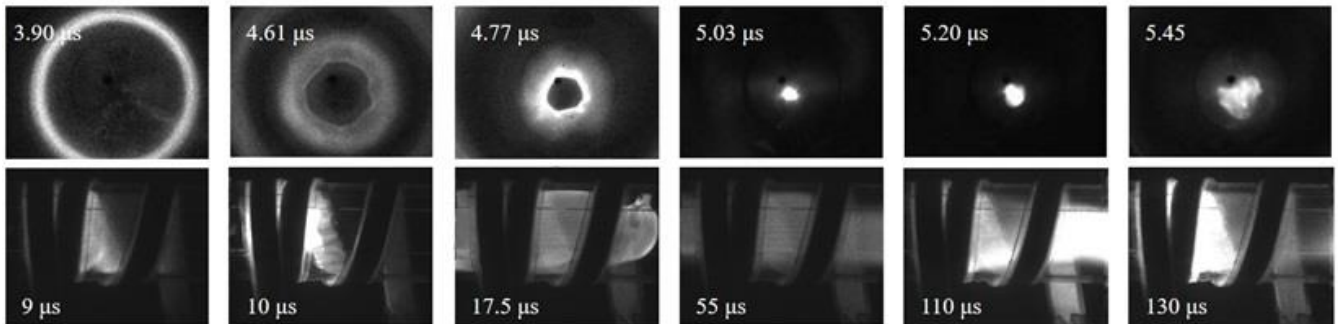
Figure 5. Axial view frame images of the light emission (**top row**) obtained at different times of plasma compression for a single-loop Theta Pinch at Hydrogen pressure of 63 Pa and at frame duration of 10 ns; transversal view frame images of light emission (**bottom row**) obtained at different times for the three-loops setup at Hydrogen pressure of 106 Pa and at frame duration of 10 ns.

(a)

(b)
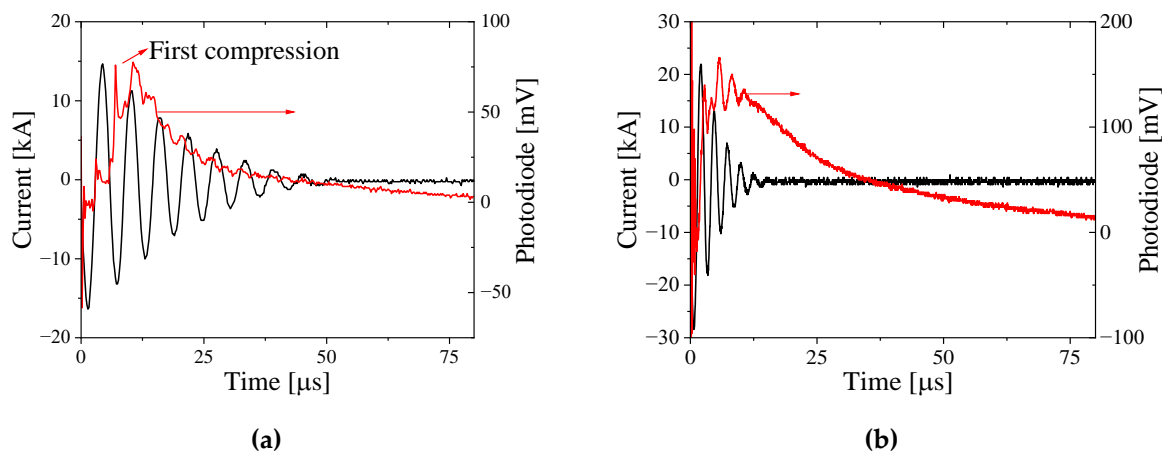
Figure 6. Typical waveforms of current (black) and photodiode light intensity (red) obtained for single-loop (**a**) and three-loop (**b**) setups for 63 Pa Hydrogen.


(a)

(b)
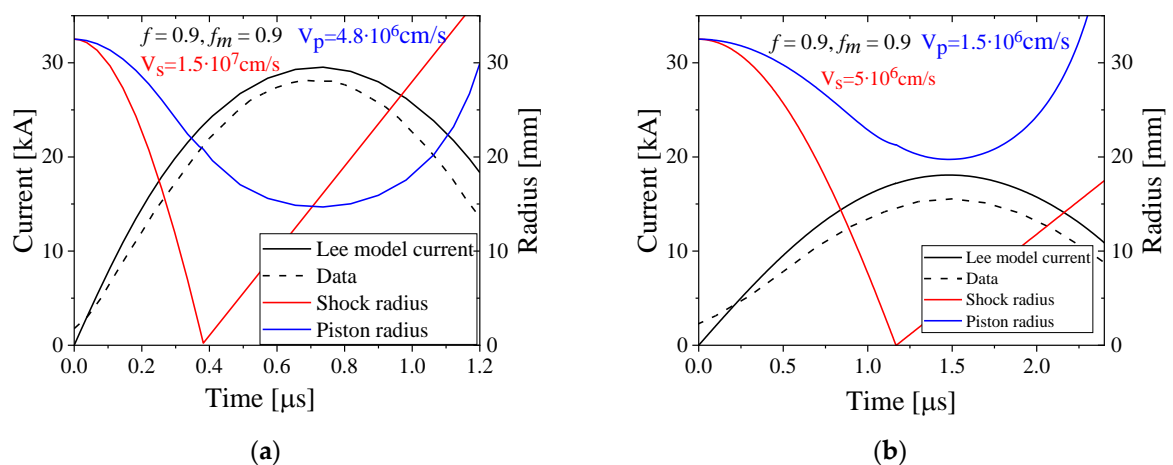
Figure 7. Lee model current (solid black) compared with the measured current (dashed black) for single-loop (**a**) and three-loop (**b**) setups and calculated shock (red) and piston (blue) radii during initial compression. He gas pressure is 63 Pa.

3.2. Microwave Cut-Off Measurements

The propagation of electromagnetic (EM) waves in the plasma in the absence of a magnetic field is possible only when the frequency of the EM waves ω_{EM} is higher than the plasma electron frequency, $\omega_p = \left(n_e e^2 / m_e \varepsilon_0 \right)^{0.5}$, where n_e is the plasma electron density, e the electron charge, m_e is the electron mass, and ε_0 is the vacuum permittivity. Here, it is assumed that $\omega_{EM} \gg \nu_{en}$, where ν_{en} is the electron-neutral collision frequency. This can be used to obtain the lifetime of plasma with a density larger than the critical density: $n_{cr} = \omega_{em}^2 m_e \varepsilon_0 / e^2$.

In this present research, a klystron (model 44151H, Hughes EDD, Torrance, CA, USA) was used as a 70 GHz continuous wave (CW) microwave source. The klystron was connected to a WR15 waveguide (50–75 GHz) with an ANTT-SGH-50-70 horn antenna (NSI-MI Technologies, Suwanee, Georgia, USA) (gain of 24.4 dBi) at its output. The antenna was located at a distance of 3 cm from the three-loop setup and positioned between the space between the loops, allowing microwaves to pass through the tube wall (see Figure 8). On the opposite side of the tube, a receiving NTT-SGH-50-70 antenna (NSI-MI Technologies) was placed at the same distance of 3 cm from the tube. This antenna was coupled with a coaxial adapter and the microwave signal was detected by a Schottky diode. In these experiments, a fast photodiode was used to provide the dynamics of light emission from the plasma.
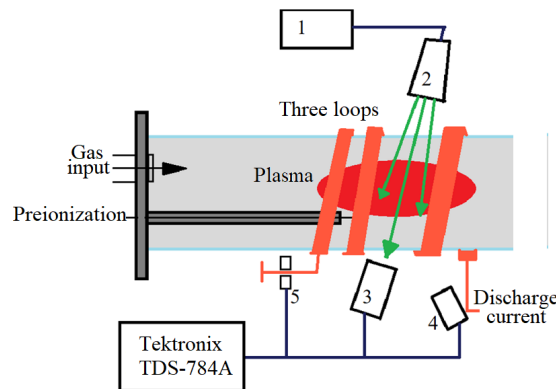
Figure 8. Microwave cutoff setup for a three-loop Theta Pinch setup: (1) 32 V DC source, (2) the klystron and antenna (70 GHz), (3) receiving antenna with the Schottky diode, (4) photodiode, (5) Pierson current monitor. Microwaves are marked as green arrows.

Using this setup, the lifetime of the plasma with $n_{cr} \geq 5 \cdot 10^{13}$ cm^{-3} corresponding to $\omega_{EM} = 70$ GHz was studied for Helium and Hydrogen plasmas, generated by TP for different gas pressures. Examples of these measurements are shown in Figure 9. Plasma with electron density $n_e \geq 5 \cdot 10^{13}$ cm^{-3} exists for ~100 μs and up to ~800 μs for Hydrogen and Helium plasmas, respectively. Moreover, increasing gas pressure leads to an increase in the plasma lifetime.
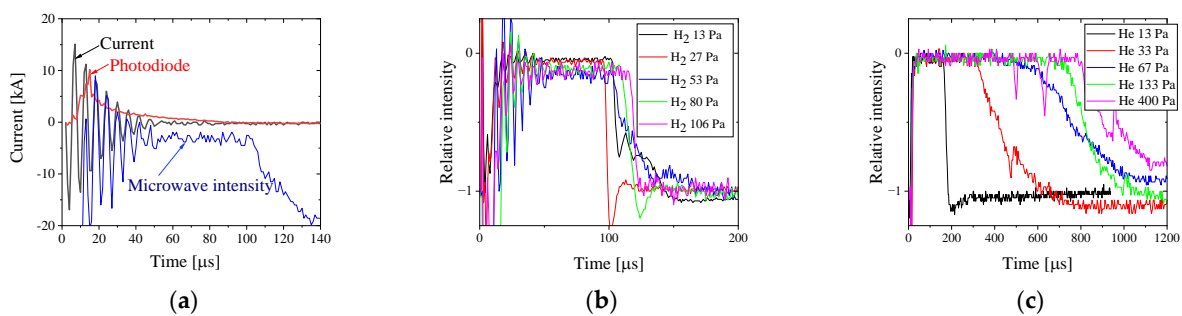
Figure 9. Typical waveforms of the discharge current, light emission, and transmitted microwave intensity (**a**) obtained for Helium at 63 Pa pressure. The transmitted microwave intensity for Hydrogen (**b**) and Helium (**c**) plasma experiments at different gas pressures. All results are for the three-loop setup.

3.3. Laser Interferometry

Since the microwave cut-off experiments only provide the lifetime of plasma with $n_e \geq n_{cr}$, laser interferometry was implemented to study the time-resolved line-integrated plasma density evolution across the tube's diameter. Laser interferometry is based on the phase shift acquired by a laser beam propagating through plasma, with respect to a reference laser beam propagating in air. The phase shift can be calculated as follows: $\Delta\phi(t) = \frac{\omega_0}{c}\left(\sqrt{\varepsilon_{pl}(t)} - 1\right)L + \Delta\phi_0$, where ω_0 is the frequency of the laser beam, L is the plasma length, c is the speed of light, $\Delta\phi_0$ is the phase shift related to the difference in two arms of the interferometer due to vibration of the optical elements, and ε_{pl} is the dielectric constant of the plasma [23]:

$$\varepsilon_{pl}(t) = 1 - \left(\frac{\omega_{pl}(t)}{\omega_0}\right)^2 = 1 - \frac{n_e(t)e^2}{\varepsilon_0 m_e \omega_0^2}, \text{ if } \nu_{en}^2 << \omega_0^2, \tag{4}$$

Thus, the plasma electron density can be calculated in terms of the phase shift:

$$n_e = \frac{4\pi\varepsilon_0 m_e c^2}{e^2}\frac{\Delta\phi_{pl}(t)}{L\lambda} = 3.55\cdot10^{19}\frac{\Delta\phi_{pl}(t),}{L(\text{cm})\lambda(\text{nm})}, \ \left[\text{cm}^{-3}\right], \tag{5}$$

where λ is the laser wavelength.

In the experiment, when two waves $\vec{E}_{1,2} = \left|\vec{E}_{1,2}\right|sin(\omega_0 t - kx + \phi_{1,2})$ are added at one point in space (at the input of the fast photodiode), the resulting wave intensity is $I = \left|\vec{E}\right|2 = I_1^2 + I_2^2 + 2\sqrt{I_1 + I_2}\cos(\Delta\phi)$. In our case, the phase shift accounting for the acoustic vibration of the optical elements is equal to $\Delta\phi(t) = \Delta\phi_{pl}(t) + \Delta\phi_0$. Therefore we use two digitizing oscilloscopes with data acquisition with two different time sweeps. The phase shift for the measured signals can be found:

$$I(t) = I_0 sin[\Delta\phi(t)] + C, \tag{6}$$

where $C = 0.5(I_{max} + I_{min})$ and $I_0 = 0.5(I_{max} - I_{min})$ obtained from the waveform are registered by the digitizing oscilloscope with a slow timescale. Here, I_{max} and I_{min} are the maximum and minimum amplitudes of slow interference signal during plasma generation. Thus, the phase shift $\Delta\phi_{pl}(t)$ is given:

$$\Delta\phi_{pl}(t) = sin^{-1}\left[\frac{I(t) - C}{I_0}\right] - \Delta\phi_0 \tag{7}$$

We used an in-house MATLAB R2023a code for signal processing, which includes FFT filtering of the noise and signal-smoothing procedures.

In this set of experiments, a Michelson interferometer was assembled (see Figure 10). The interferometer consists of either a red laser (λ = 632.8 nm, P = 15 mW) or a green laser (λ = 532 nm, P = 200 mW) (1), beam splitter (2), two mirrors (3,4), ND filter 0.3 (7), bandpass filter (λ = 632 ± 1 nm or 530 ± 5 nm) (5), and a fast photodiode FDS010 ThorLabs (Newton, NJ, USA) (1 ns time resolution) (6). A laser beam is split between mirrors (3) and (4) using a beam splitter. One of the beams propagates through a Pyrex tube where the plasma is generated. The reflected laser beams (Ray 1 and Ray 2) from mirrors (3) and (4) are returned and combined by the beam splitter and are registered by a fast photodiode. Ray 2 has a phase shift relative to Ray 1 due to a change in the plasma density, resulting in an interference signal at the diode output.

Waveforms of the voltage from the fast photodiode (6) are registered by two digitizing oscilloscopes: Tektronix TDS-2014C and Tektronix TDS-784A (Beaverton, OG, USA). The Tektronix TDS-2014C acquires a signal with a slow time sweep (250–2500 μs/div) and the Tektronix TDS-784A does so with a faster time sweep (20–50 μs/div). Thus, we obtain an interference waveform due to the low-frequency vibration of optical objects (mirrors,

etc.) using the Tektronix TDS-2014C oscilloscope. The signal from the photodiode, which collects the plasma light, allows us to obtain the initial maximal and minimal amplitudes of the interference signal, which appear due to the acoustic motion of mirrors at the time of the plasma density evolution.
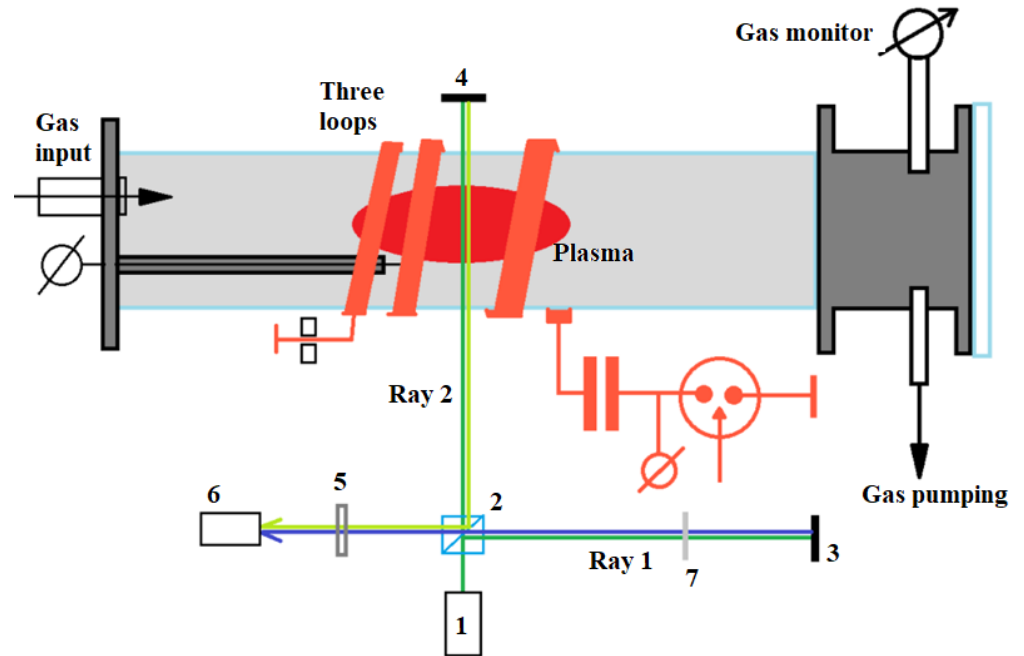
Figure 10. Michelson interferometer set up for average plasma density measurements for a three-loop Theta Pinch experiment. (1) Laser; (2) beam splitter; (3) and (4) mirrors; (5) bandpass filter matching the laser wavelength; (6) photodiode; (7) ND filter.

Interference waveforms measured in a single shot with the two oscilloscopes on the ms and µs timescales are shown in Figure 11a,b. On the ms timescale, low-frequency oscillations are seen due to the acoustic motion of the mirrors. These provide the interference amplitude and phase difference over the plasma density's evolution time. On the µs timescale, with plasma formation, a change in the amplitude of the interference signal, caused by the phase shift of Ray 2, is registered. This effect happens due to the plasma's rising dielectric index due to its density increase. The results for 53 Pa Hydrogen plasma density for the three-loop setup are shown in Figure 11c.
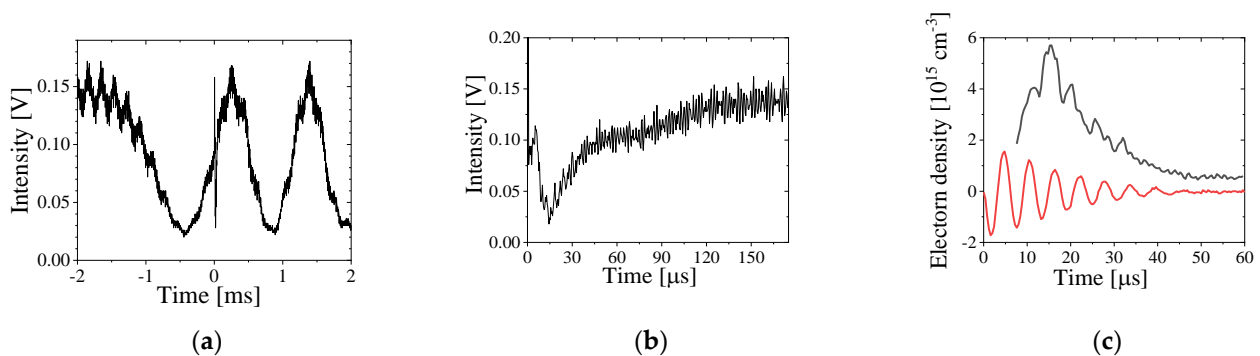
Figure 11. (**a**) Interference waveform measured on a ms timescale. (**b**) Interference waveform measured on a 100 µs timescale. (**c**) Electron density (black) and discharge current in relative units (red) for 53 Pa Hydrogen plasma and a three-loop setup.

In Figure 12, we present the results of the average electron density evolution in Hydrogen and Helium plasmas. This value of density was obtained considering that in the

analysis, the laser path length is two times the diameter of the tube. It is understood that this assumption gives low values of the density of the plasma, which oscillates and compresses to a much smaller radius than the tube radius. For Hydrogen, the maximal plasma density increases up to 6×10^{15} cm^{-3} in the pressure range of 53–105 Pa, respectively. Additionally, the increase in pressure leads to a slower decay in the plasma density. Furthermore, the results obtained using green (see Figure 12a) and red (see Figure 12b) lasers agree quite well. For Helium plasma, the maximal electron density of ~10^{16} cm^{-3} was estimated at 131 Pa (see Figure 12c). Here, we emphasize again that this method gives the line integrated plasma density averaged along the length of the laser propagation, resulting in a significantly larger plasma density at the time when the implosion is expected.
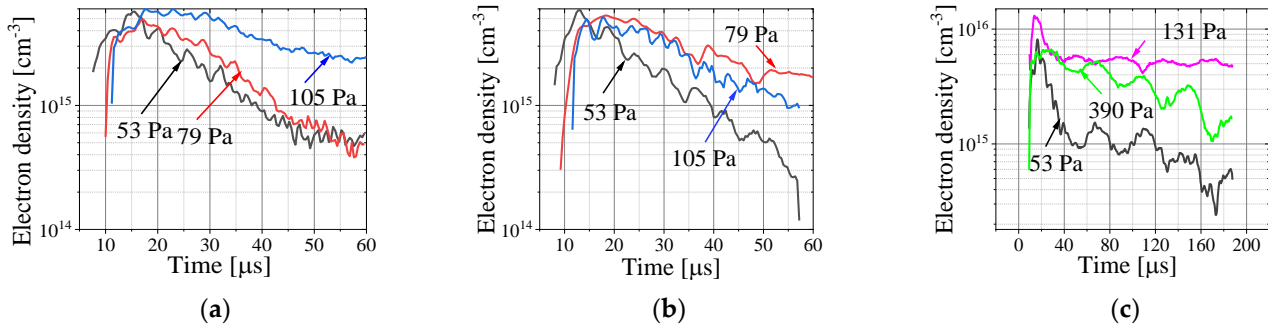
Figure 12. Electron density evolution at different pressures of Hydrogen plasma using the green laser (**a**), red laser (**b**), and (**c**) Helium plasma (green laser) for a three-loop Theta Pinch setup.

3.4. Results of Visible Spectroscopy

Plasma spectroscopy utilizes high-resolution spectral line measurements of the emitted plasma light by which the plasma density and temperature can be estimated. Here (see Figure 13), the light emitted from the plasma was collected by a 100 mm in diameter lens and focused (170 mm focal length) onto a 100 μm-wide slit of a 1 m-long focus spectrometer with a grating of 2400 grooves/mm. At the output of the spectrometer, a fast-framing 4QuikE intensified camera was installed (see Figure 13). To obtain reliable spectral line profiles, the duration of the camera frame in these experiments was 100 ns. Thus, the density and temperature obtained by analyzing the spectral lines should be considered average values during the exposure time. Spectral lines were obtained at various times relative to the beginning of the discharge current by controlling the time delay of the camera's trigger time. Spectral calibration of the spectrometer at Hα (656.28 nm) and Hβ (486.13 nm) spectral lines using Hydrogen spectral lamps resulted in $R_{H_\alpha} = 0.1075$ Å/pixel and $R_{H_\beta} = 0.153$ Å/pixel. Using this spectral resolution, the instrumental Full Width at Half Maximum (FWHM) broadening of Hα and Hβ spectral lines was found to be $\Delta\lambda_{inst H_\alpha} = 0.432$ Å and $\Delta\lambda_{inst H_\beta} = 0.533$ Å.

For Hydrogen plasma, the main effects responsible for line broadening are Doppler broadenings due to Hydrogen atom temperatures and Stark broadening created by the electric fields of the electrons and ions. To distinguish between the contributions of these two effects, the following algorithm was applied. The H_α line Stark broadening is smaller than the H_β line Stark broadening for the same density of the plasma [23]. However, the Doppler broadening of the H_α line is larger than that of H_β. In general, assuming a Maxwellian energy distribution, the Doppler broadening of the spectral line due to the temperature of neutrals can be calculated as follows [24]:

$$\Delta\lambda_D = 2\lambda_0 \sqrt{2\ln 2 \frac{k_B T_i}{m_i c^2}}, \tag{8}$$

where $\Delta\lambda_D$ is the Doppler FWHM of the spectral line, λ_0 is the central wavelength of the line, k_B is the Boltzmann constant, T_i is the ion or neutral atom temperature, m_i is the mass of the ion or neutral atom, and c is the speed of light in a vacuum.
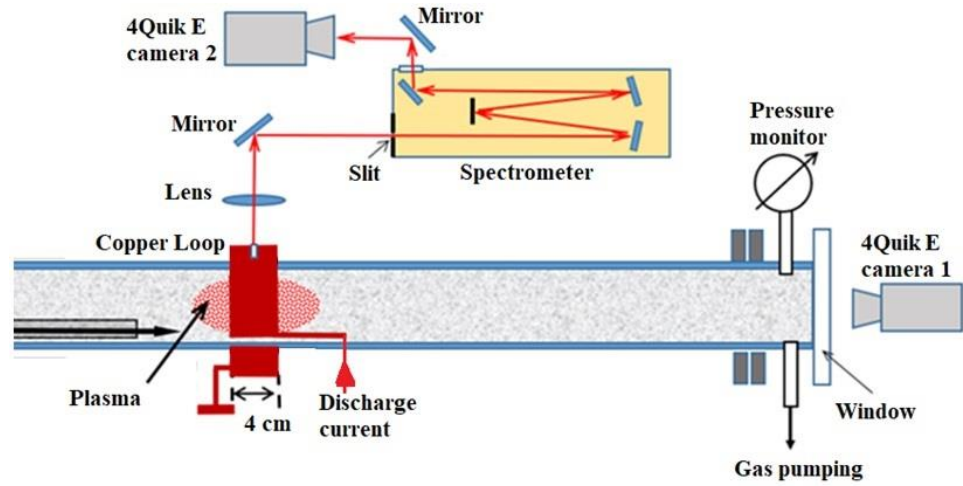
Figure 13. Spectroscopy setup. A single-loop setup.

First, we assume that the Stark broadening of the H_α line is much smaller than the Doppler broadening. Thus, considering the instrumental broadening of the spectral line $\Delta\lambda_{inst}$, the Doppler line broadening of the H_α line was calculated: $\Delta\lambda_{DH_\alpha} = \sqrt{\Delta\lambda_{exp}^2 - \Delta\lambda_{instH_\alpha}^2}$, where $\Delta\lambda_{exp}$ is the FWHM of the experimentally measured spectral line. Next, the temperature of Hydrogen atoms was calculated. This value of the temperature was used to calculate the H_β line Doppler broadening $\Delta\lambda_{DH_\beta}$, allowing, in turn, to calculate a Gaussian FWHM of the H_β line as $\Delta\lambda_{G\beta} = \sqrt{\Delta\lambda_{DH_\beta}^2 + \Delta\lambda_{instH_\beta}^2}$. Now, considering that the Stark effect contributes to the H_β line broadening, the line becomes characterized by a Voigt profile in which FWHM is $\Delta\lambda_V \approx 0.5346\Delta\lambda_L + \sqrt{0.2166(\Delta\lambda_L)^2 + (\Delta\lambda_{G\beta})^2}$ [25]. Solving this quadratic equation, the Lorentzian FWHM $\Delta\lambda_{LH_\beta}$ of Hβ was found, given the known values of $\Delta\lambda_V$ and $\Delta\lambda_G$. Next, the electron density was calculated using the empirical relation [24]:

$$n_e = 10^{17}\left(\frac{\Delta\lambda_{LH_\beta}\,[\text{nm}]}{4.8}\right)^{1.468}\left[\text{cm}^{-3}\right] \tag{9}$$

This density can then be used to find the Stark contribution $\Delta\lambda_{LH_\alpha}$ to the H_α line FWHM [25]:

$$\Delta\lambda_{LH_\alpha}\,[\text{nm}] = 1.098\left(\frac{n_e\left[\text{cm}^{-3}\right]}{10^{-17}}\right)^{\frac{1}{1.471}} \tag{10}$$

With this contribution, a new ion temperature of Hydrogen was found, and the process was repeated until the convergence of the density and temperature obtained for H_α and H_β was reached. The results of this analysis for different Hydrogen gas pressures are presented in Figure 14. The electron density reached $\sim 8 \times 10^{15}$ cm^{-3} within the first $\sim$15 μs, followed by a decrease within 70 μs to $<10^{15}$ cm^{-3}. The Hydrogen temperature reached $\sim$25 eV and later decreased to $\sim$3 eV. A relatively large temperature of the Hydrogen can be explained by a possible Doppler shift of the spectral lines due to radial motion of the Hydrogen atoms, resulting in a thermal temperature that can be significantly smaller. Also, using the calculated plasma electron density, we estimated the electron temperature T_e using another approximate expression [25]:

$$\log(n_e) = 22.578 + 1.478 \times \log\left(\Delta\lambda_{LH_\beta}\right) - 0.144 \times \log\left(\Delta\lambda_{LH_\beta}\right)^2 - 0.1265 \times \log(T_e) \tag{11}$$

The temperature of electrons was $\leq$2.5 eV, which indicates a small degree of ionization of the neutral gas.
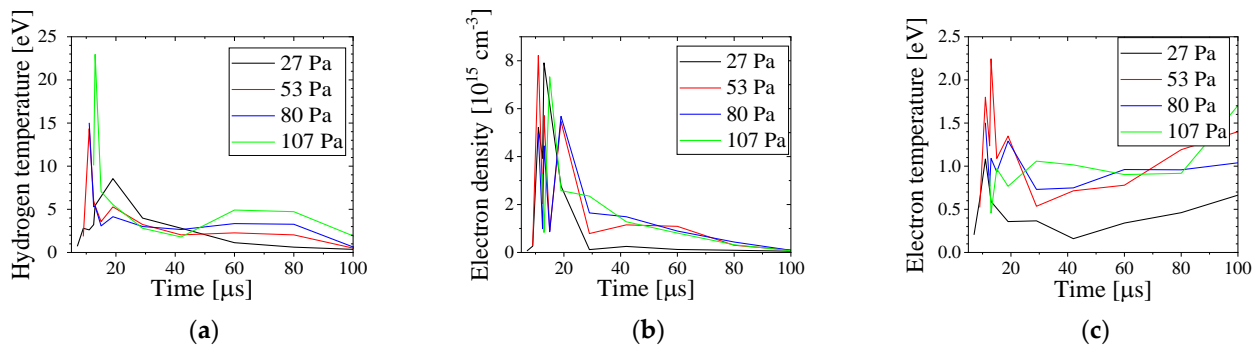
Figure 14. (**a**) Ion temperature, (**b**) electron density, and (**c**) electron temperature calculated for Hydrogen plasma at various gas pressures for the three-loops setup.

Additionally, assuming a Boltzmann distribution of the quantum states population, the plasma electron temperature can be found using the ratio between H_α and H_β spectral line integral intensities [24]:

$$\frac{I_\alpha}{I_\beta} = \frac{\omega_{32}^\alpha A_{32}^\alpha g_3^\alpha}{\omega_{42}^\beta A_{42}^\beta g_4^\beta} e^{-\frac{E_{3,\alpha} - E_{4,\beta}}{k_B T_e}} \tag{12}$$

Here, I_i is the integral intensity of the spectral line, ω_{ij} is the frequency of the emitted photon for the $i \to j$ transition, A_{ij} is the Einstein coefficient for the same transition, g_i and E_i are the degeneracy and energy of the level, respectively, and T_e is the electron temperature. This estimate also results in $\leq$2 eV electron temperatures.

In the case of Helium plasma, the electron temperature was estimated using a Boltzmann plot [26]:

$$\ln\left(\frac{\varepsilon_{ji}\lambda_{ji}}{A_{ji}g_j}\right) = -\frac{1}{k_B T_e}\Delta E + C \tag{13}$$

Here, λ_{ji} is the wavelength of the emitted photon, ε_{ji} is the energy difference between the upper and lower energy levels, g_j is the degeneracy of the upper level, and C is a constant.

The spectral lines of He I 388, 402, 501, 587, and 706 nm were measured prior to the plasma compression (~4 µs) and during compression (~5 µs). In Figure 15, a linear fit of the Boltzmann plot is presented, resulting in an electron temperature of <1.5 eV, similar to the results with Hydrogen plasma.
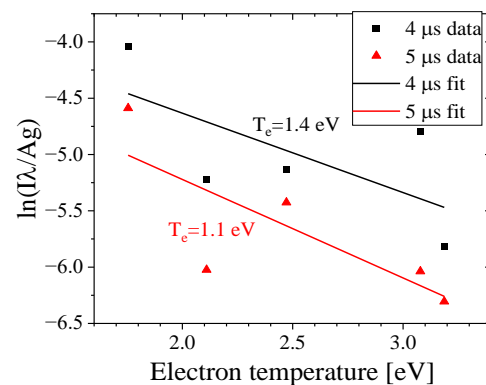
Figure 15. Electron temperatures estimated 4 and 5 µs after the start of the current using a Boltzmann plot.

Moreover, for Helium plasma, we used the forbidden transition 2^3P–4^3F of the He I 447.1 nm line to obtain the plasma electron density using the following relations [27,28]:

$$\log n_e = 22.563 + 1.658 \log\frac{F}{A} + 0.257\left(\log\frac{F}{A}\right)^2, \tag{14}$$

$$\log n_e = 21.041 + 3.372\frac{D}{A} - 1.38\left(\frac{D}{A}\right)^2, \tag{15}$$

$$\log n_e = 23.056 + 1.586\log(s - 0.156) + 0.225(\log(s - 0.156))^2 \tag{16}$$

Here, n_e is the electron density in m^{-3}; F and A are the amplitudes of the forbidden and allowed lines, respectively; D is the amplitude of the dip between the lines; and s is the difference in wavelength between the lines in nm. A comparison between the three relations shows consistent results (Figure 16).
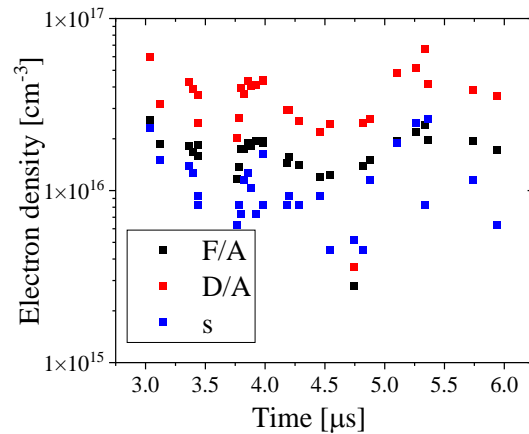
Figure 16. Electron density calculated using the three relations involving the forbidden–allowed transition of the 447.1 spectral line of the He I atom.

3.5. Thomson Scattering

During plasma compression, the electron energy distribution function changes over time. The most appropriate method to study the evolution of this distribution function is the use of Thomson scattering measurements. Calculating the scattering of electromagnetic (EM) radiation in the plasma, the electron oscillations due to rapidly changing fields of EM waves need to be considered. These oscillations of the plasma electrons and the resulting electron trajectories are very complex, even when it is assumed that the electrons do not interact with each other. As an EM wave propagates through the plasma, each electron oscillates according to the alternating electrical field of the wave. For a dilute plasma, one can neglect the Coulomb interaction between electrons and ions, and therefore, the scattered EM waves will only be broadened due to electron temperature (Doppler effect), resulting in a Gaussian broadening of the scattered spectral line FWHM, which can be used to calculate the electron temperature.

For dense plasmas, the fields produced by neighboring electrons and ions cannot be neglected. Electron and ion density fluctuations contribute small Coulomb perturbations to the electron trajectories. Therefore, the scattered photons are not considered to interact with each electron, but rather, are scattered by these electron density fluctuations. These fluctuations lead to various features in the scattering spectrum. In order to distinguish between the different behaviors of the scattered radiation, the Salpeter parameter [29] is used, defined as $\alpha = \frac{1}{\Delta k \lambda_D} = \frac{\lambda}{4\pi\lambda_D\sin(\theta/2)}$, where $\Delta k = \left|\vec{k}_s - \vec{k}_0\right| \cong 2k_o\sin\left(\frac{\theta}{2}\right)$, λ is the wavelength of the laser, $\vec{k}_0 \approx \vec{k}_s$ are the wavevectors of the incident and scattered photons, $\theta = 90^0$ is the angle between the incident and scattered wave vectors, and λ_D is the Debye radius of the plasma. For $\theta = 90^0$ and $\lambda = 5320\dot{A}$, one obtains $\alpha = 0.87(n_e/T_e)^{1/2}$, where electron density is in units of 10^{16} cm^{-3} and electron temperature is in eV.

The value of Δk is a fixed parameter determined by the observed angle of the scattered light and the Debye radius $\lambda_D \sim (T_eT_i/n_e(T_e + T_i))^{1/2}$, which depends on the electron density n_e and electron T_e and ion T_i temperatures. A large value of λ_D corresponds to low-density, low-temperature plasma. For this case, Coulomb interactions of charged

particles are weak, giving a Salpeter parameter value of $\alpha \ll 1$. In this regime, electrons are uncorrelated (electrons are moving almost freely in the plasma), and this is the regime of non-collective scattering. This is an analog to saying that the laser wavelength $\lambda_D \gg \lambda$ is much smaller than the Debye length.

However, when $\lambda \geq \lambda_d$, corresponding to the condition of $\alpha \geq 1$, collective effects are to be considered. Laser photons are not considered to be scattered by free electrons but by a perturbed electron cloud density of a specific electron plasma frequency and by electrons coupled to ions in the Debye sphere. Thus, the spectrum of the scattered light has two components, labeled the electron and ion parts. The electron part, having a higher frequency, is shifted to both sides of the central laser wavelength due to collective plasma electron frequency oscillations. Assuming that this process is comparable to an inverse Compton scattering of the laser photon from an ensemble of coupled electrons oscillating with ω_{pe}, the plasma electron density can be roughly estimated by measuring the shifted $\Delta\lambda$ of the electron part: $\Delta\lambda = 2\pi c/\omega_{pe}$. The ion part appears due to the photons scattered by the electrons coupled to ions in the Debye sphere. Ion thermal motion and ion acoustic waves, manifested as plasma density perturbations, affect the ion-coupled electrons, which experience these displacements. This results in the broadening of the central ion part, as well as in the appearance of two symmetrical intensity peaks when photon scattering from ion acoustic oscillations is dominant. The frequency separation of these two peaks can be used to estimate the electron temperature. Analyzing the electron density fluctuation yields to an expression of the spectral density function (SDF) [29]:

$$S\left(\vec{k},\omega\right) = \frac{2\pi}{k}\left|1 - \frac{\chi_e}{\epsilon}\right|^2 f_{e0}\left(\frac{\omega}{k}\right) + \frac{2\pi Z}{k}\left|\frac{\chi_e}{\epsilon}\right|^2 f_{i0}\left(\frac{\omega}{k}\right) \qquad (17)$$

Here, $\epsilon = 1 + \chi_e + \chi_i$ is the plasma dielectric constant and χ is the electron (e) and ion (i) electric susceptibility, respectively. Assuming that f_{q0} is the Boltzmann distribution, one can see that when $\alpha \ll 1$, the spectrum is just a Gaussian function due to Doppler broadening of the scattered photons by free electrons having finite temperature. However, when α is not negligible, one obtains a high-frequency feature owing to the electron plasma frequency. Additionally, the low-frequency ion feature is no longer Gaussian and depends on the plasma ion and electron temperatures and density.

In our experiments, a Surelite III Nd:YAG laser's second harmonic at 532 nm with 4 ns pulse duration and 350 mJ/pulse energy is focused at the location of the plasma compression region. To minimize parasitic scattered light of the laser beam from the walls of the tube, collimators and a graphite damper were used (see Figure 17). Scattered light was collected perpendicular to the beam's path into a spectrometer. In these experiments, for each feature in the SDF, different spectrometers were used. With plasma electron density estimated to be $\geq 10^{16}$ cm^{-3} during compression, as found in previous experiments, the Salpeter parameter is calculated as $\alpha \geq 0.1$ for electron temperatures < 75 eV. Thus, at compression, the plasma is dense, and collective plasma behavior should be considered. The central line profile was observed using the same spectrometer used in the emission spectroscopy experiments, and the electron features were observed using a 25 cm focal length spectrometer with 600 grooves/mm corresponding to a resolution of 1.7 A/pixel.

The experimentally obtained spectral line profiles of the laser's scattered light are presented in Figure 18. These line profiles were obtained in the same way as all spectroscopic line profiles described in the manuscript. Namely, we used a ~10 ns duration of the frame of the 4QuikE camera installed at the output of the spectrometer. Additionally, images of the spectrum at the output of the spectrometer with the same duration of the frame were obtained with only the laser firing and with only plasma without a laser. These images were used to clean the Thompson scattered signal. In Figure 18a electron features, presented as symmetric peaks, appearing with ~2 nm and 5 nm shifts from the central line are visible. The electron part's study by numerical calculation of the SDF shows that the best fit of these peaks can be obtained for plasma densities ~5 × 10^{16} cm^{-3} and ~5 × 10^{17} cm^{-3} with electron temperatures ~1.7 eV and ~0.5 eV, respectively. Central line analysis (see

Figure 18b) confirms the spectroscopic results with ion temperature reaching 20–25 eV during the plasma's main compression for both Hydrogen and Helium at 53 Pa pressure.
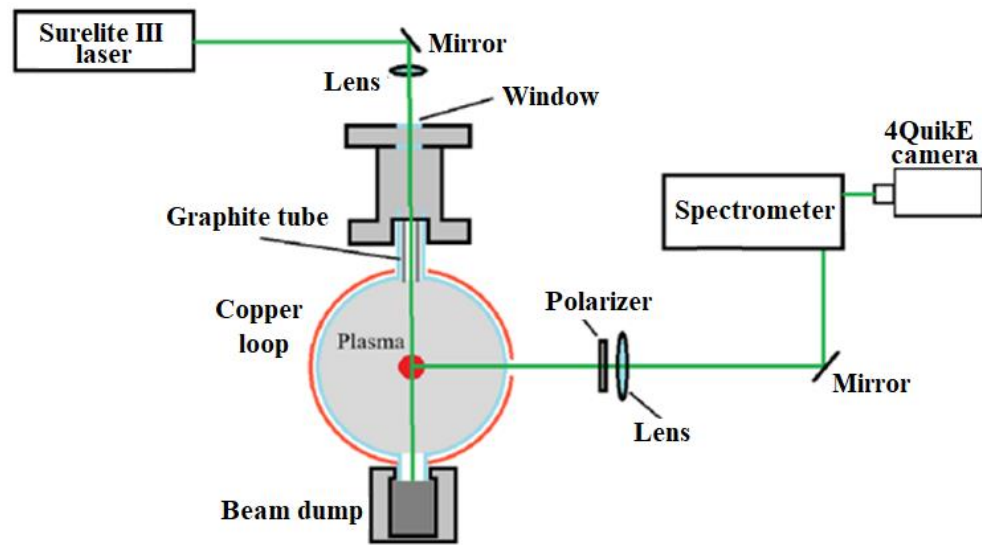

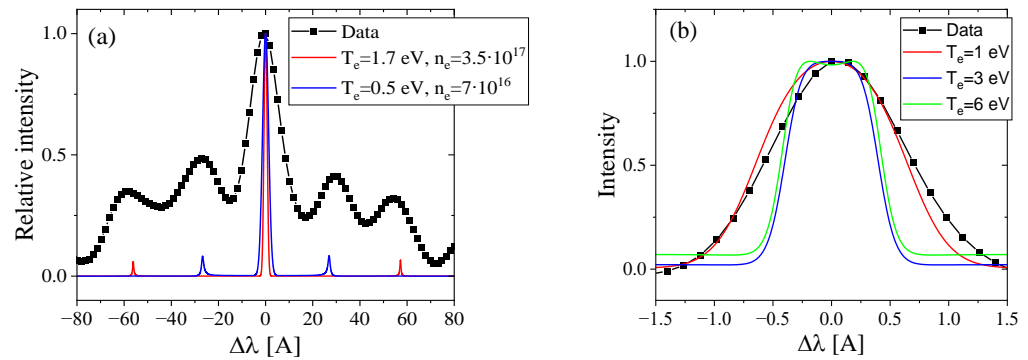**Figure 17.** Setup for Thomson scattering experiment. Single-loop setup.

Figure 18. (**a**) Thomson scattering spectrum measured for 53 Pa Hydrogen gas pressure at the time of plasma compression with ~20 eV ion temperature (black) compared to the numerical SDF with the same ion temperature for different electron temperatures and densities. (**b**) The central spectral feature measured with the high-resolution spectrometer at the same time and same gas pressure (black) compared to the SDF calculated for $n_e = 5 \cdot 10^{16}$ cm^{-3} for different T_e.

3.6. Laser-Induced Fluorescence (LIF)

We applied LIF to study neutral atom temperatures utilizing a four-energy quantum level scheme for He plasma. In a Helium atom, a 667.82 nm photon excites an electron transition from the 2^1P level to the 3^1D level. Electrons of the 3^1D level populate the 3^1P level and spontaneously decay from this level to the 2^1S level, emitting a 501.6 nm photon. Changing the wavelength of the dye laser to ~667.82 nm and measuring the intensity of the 501.6 nm 3^1P–2^1S transition fluorescence photons, He atoms with different velocities along the laser beam direction were observed.

The experimental setup for LIF measurements is shown in Figure 19. A ND6000 dye laser was pumped by a Nd:YAG Surelite III laser's second harmonic, 532 nm, of ~4 ns pulse duration and ~350 mJ/pulse energy. The dyes used are 176 mg/liter DCM dissolved in DMSO (Dimethyl sulfoxide) in the oscillator and 24 mg/liter DCM dissolved in methanol in the amplifiers, resulting in an output pulse of ~4 ns duration with ~4.4 mJ/pulse energy at 667.82 nm. The dye laser beam passes an expander consisting of a 3 mm diameter iris and 2.5 cm and 5 cm focal length lenses to produce a beam of 6 mm diameter. After the expander, the ~2.5 mJ/pulse energy laser beam was directed perpendicularly to the tube

axis. The fluorescence photons were collected using a 170 mm focal length lens to a 1 m focus spectrometer with a grating of 2400 grooves/mm. The spectral resolution of the setup was calibrated using Oriel spectral lamps and a 4QuikE intensified camera installed at the output of the spectrometer. The calibration factor was 0.123 A/pixel resolution at 501 nm. The spectrometer acts as a spectral filter with a range of ± 3.5 nm. In experiments with plasma, the intensity of the spectral line at the output of the spectrometer was measured using a Hamamatsu R988U-210 photo multiplier tube (PMT) (Hamamatsu City, Shizuoka Prefecture, Japan) with 580 V MCP gain.
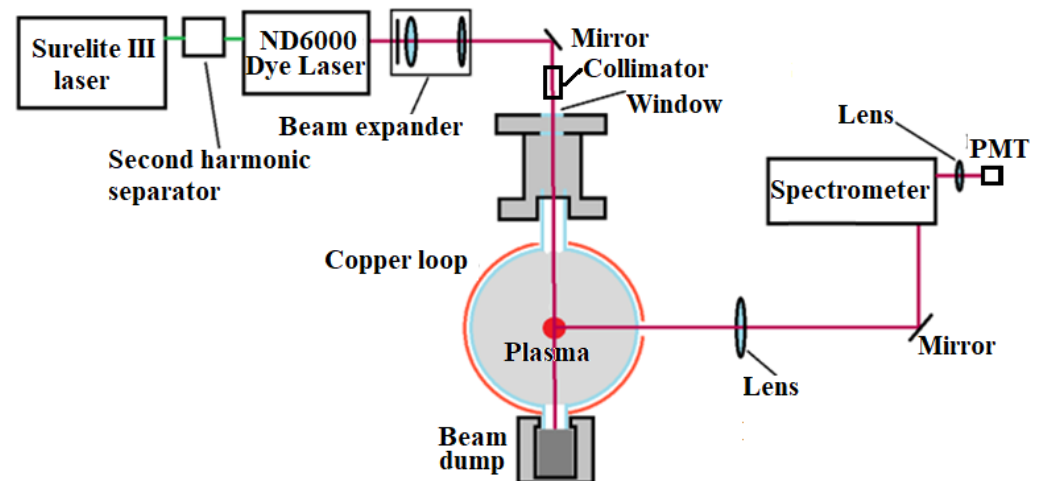

Figure 19. Experimental setup for Helium LIF measurements. Single-loop setup.

In He plasma, measurements at various times of plasma evolution showed that the LIF signal disappears ~250 ns prior to the first plasma compression and reappears ≥ 50 μs after this compression. In these experiments, the He gas density in the tube was $\sim 3.7 \cdot 10^{16}$ cm^{-3}. The results of laser interferometry and spectroscopy showed that the plasma electron density is in the range $\leq 3 \cdot 10^{16}$ cm^{-3} at a time close to the plasma compression. Therefore, it is reasonable to assume that the LIF signal's disappearance is due to the low density of neutrals in the plasma close to its compression time, and it reappears as the neutral density rises with plasma recombination. LIF measurements were carried out at ~300 ns before the plasma's first compression and at ~60 μs and ~100 μs after the compression. To avoid saturation of the LIF signal, which results in artificial spectral line broadening, we obtained the dependence of the LIF signal amplitude on the time delay of the Q-switch of the Surelite laser, which determines the output energy of the laser beam (see Figure 20). At ~290 μs time delay, the LIF signal saturates. Thus, a 330 μs Q-switch delay was chosen, corresponding to ~1 mJ/pulse energy of the dye laser.

Fluorescence spectral line intensity profiles obtained at 60 μs and 100 μs of the temporal plasma evolution are shown in Figure 21. At these times, far from compression, the plasma can be considered in thermal equilibrium so that the spectral lines can be analyzed by using only Doppler broadening. Figure 21a,b demonstrates that the He atom temperature remains stable with 0.36 ± 0.5 eV to 0.46 ± 0.6 eV at 60 μs and 100 μs, respectively. Close to compression, the plasma dynamics are more complicated since spectral line broadening consists of a Doppler shift due to plasma propagation towards the axis and Doppler broadening due to the finite plasma ion temperature. Thus, we can consider only an effective temperature of the He I atoms. Here, we assumed that the temperatures of He II and He I are equal due to high collision frequency. Figure 21c shows that the He I spectral lines obtained 325 ns, 300 ns, and 275 ns prior to compression resulting in effective temperatures of 8 eV, 23 eV, and 30 eV, respectively.
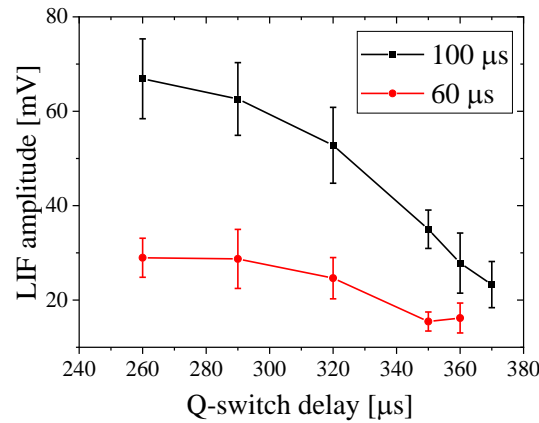
Figure 20. Dependence of the LIF amplitude measured at 100 μs and 60 μs after the plasma compression vs. the Q-switch delay time.

(**a**)　　　　　(**b**)　　　　　(**c**)
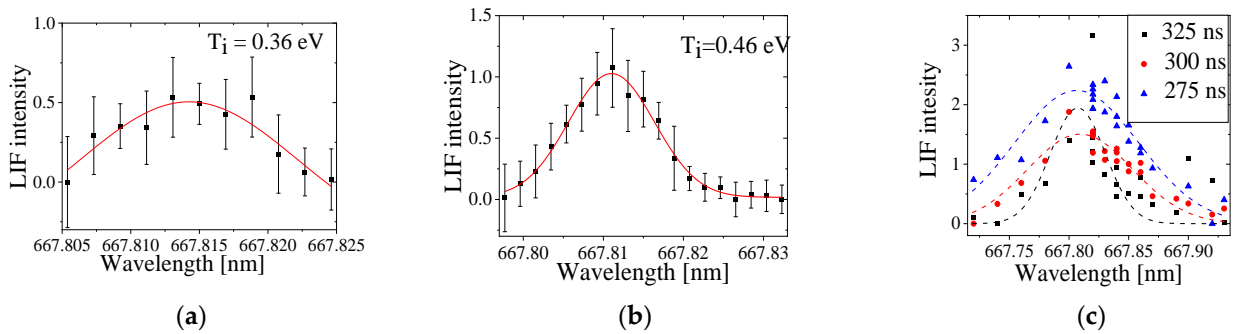
Figure 21. LIF spectral line profiles measured at 60 μs (**a**) and 100 μs (**b**) after the plasma compression and at ~275 ns, ~300 ns, and ~375 ns before the plasma compression (**c**).

For Hydrogen plasma, LIF was carried out by changing the wavelength of the dye laser close to the H_α spectral line and measuring the change in intensity of this spectral line. In these experiments, we first measured the H_α intensity without the dye laser as the background intensity. Then, with the dye laser, this background intensity was subtracted from the PMT signal, resulting in the LIF profile of the H_α spectral line (see Figure 22). These measurements, carried out at various times of the plasma evolution, show that Hydrogen atom temperature does not exceed <2 eV at the time of the plasma compression.

(**a**)　　　　　(**b**)　　　　　(**c**)
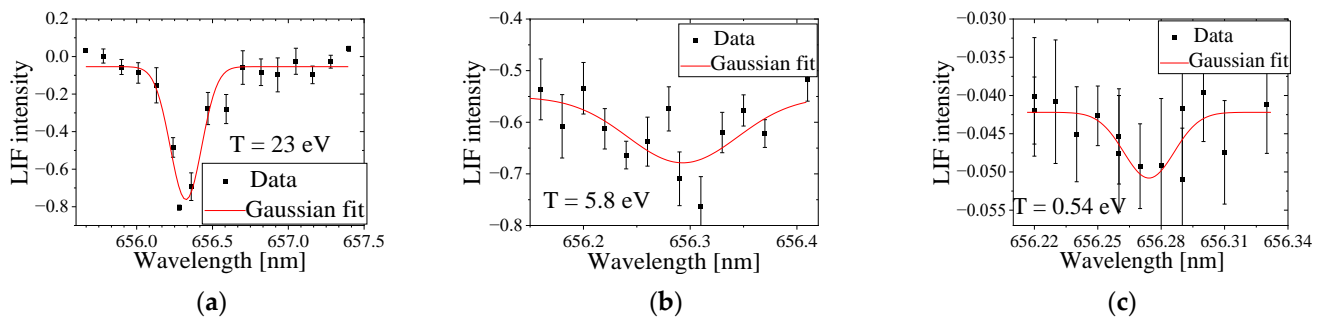
Figure 22. LIF intensity of H_α vs. the wavelength of the dye laser at different time delays relative to the first plasma compression: (**a**) 300 ns prior to plasma compression, (**b**) at the time of the plasma compression, and (**c**) 40 μs after the plasma.

Here, let us note that in the case of LIF measurement of He I atoms, the increase in the intensity of the 501.6 nm spectral line is obtained because of the increased population of 3^1P and, respectively, increased spontaneous emission (fluorescence) of the 3^1P–2^1S transition. The population of 3^1P is amplified due to 3^1D–3^1P-level electron transitions. The latter is

due to dye laser 667.82 nm photons, which excite an electron transition from the 2^1P level to the 3^1D level. Thus, one obtains an increase in the intensity of the 501.6 nm spectral line above its spontaneous emission level during the dye laser beam.

In the case of Hydrogen plasma, the H_α, $n_3 \rightarrow n_2$ transition was used for LIF measurements, and a decrease in the intensity of the light emission was obtained when the scan by the dye laser around 656.28 nm was carried out. At present, we do not know the exact explanation of this result. We can mention that the decrease in LIF intensity of H_α also was obtained in earlier research [30] of recombining rather high-density Hydrogen plasma. This effect was explained by the inverse population of n = 3 level. Another explanation can be related to the specific nature of laser interaction. Namely, resonance electron de-excitation of n = 3 level by dye laser photons is accompanied by emission of photons with the same polarization and in the same direction of propagation as the laser photons. Thus, in the direction of observation, which is transverse to the laser beam direction, one obtains a decrease in the H_α intensity as compared to the spontaneous emission of this transition. Therefore, one can consider that in the case of a rather dense plasma with several eV electron temperature levels and sufficiently high Boltzmann population of quantum levels, this effect can be considered as well. It is understood that precise collision-radiative modeling is required to determine the phenomenon responsible for the obtained decrease in H_α intensity, but this is beyond this research.

4. Summary

In this article, we presented results characterizing a small and compact Theta Pinch using different non-perturbing, time and space-resolved diagnostics. In addition to electrical measurements of the discharge current, the results of various diagnostic methods and their analysis were presented. The methods we used were microwave cut-off, laser interferometry, visible spectroscopy, Thomson scattering, and LIF. Using these methods, plasma density and temperature evolution were obtained, and the results from different diagnostic methods were found to be in satisfactory agreement. In Table 1, we present the maximal values of the plasma density and temperature of ions and electrons obtained with these diagnostic methods in setups with three-loop and single-loop Theta Pinch at the time of plasma compression. One can see a satisfactory agreement between plasma densities and temperatures measured by the interferometry and spectroscopy methods. The results of Thomson scattering show almost the same temperature of ions and electrons in the spectroscopy results but a significantly larger density of the plasma. The latter can be explained due to the local density measured by Thomson scattering, whereas the spectroscopy measurements give an average along sight of view density of the plasma.

Table 1. Maximal values of the Hydrogen and Helium plasma density and temperature obtained with different diagnostics applied in experiments with three-loop and single-loop Theta Pinch setups.

	Hydrogen Plasma n_e [cm^{-3}]	Hydrogen Plasma T_i [eV]	Hydrogen Plasma T_e [eV]	Helium Plasma n_e [cm^{-3}]	Helium Plasma T_i [eV]	Helium Plasma T_e [eV]
MW cutoff (three-loop Theta Pinch)	$\geq 5 \times 10^{13}$	-	-	$\geq 5 \times 10^{13}$	-	-
Interferometry (three-loop Theta Pinch)	$(6 \pm 1) \times 10^{15}$	-	-	$(1.3 \pm 0.2) \times 10^{16}$	-	-
Spectroscopy (single-loop Theta Pinch)	$(8 \pm 2) \times 10^{15}$	23 ± 5	2.3 ± 1.3	$(2.2 \pm 1.3) \times 10^{16}$	-	1.4 ± 1.1
Thompson scattering (single-loop Theta Pinch)	$(2.1 \pm 1.4) \times 10^{17}$	22 ± 2	1.1 ± 0.5	$(2.1 \pm 1.4) \times 10^{17}$	22 ± 2	1.1 ± 0.6
LIF (single-loop Theta Pinch)	-	23 ± 6	-	-	30 ± 7	-

Thus, using these diagnostics, the parameters of the plasma in the device being developed by the nT-TAO company can be studied with high reliability.

References

1. Green, T.S. Evidence for the containment of a hot, dense plasma in a theta pinch. *Phys. Rev. Lett.* **1960**, *5*, 297–300. [CrossRef]
2. Jahoda, F.C.; Little, E.M.; Quinn, W.E.; Ribe, F.L.; Sawyer, G.A. Plasma Experiments with a 570-kJ Theta-Pinch. *J. Appl. Phys.* **1964**, *35*, 2351–2363. [CrossRef]
3. Taylor, J.B.; Wesson, J.A. End losses from a theta pinch. *Nucl. Fusion* **1964**, *5*, 159–161. [CrossRef]
4. Little, E.M.; Quinn, W.E.; Sawyer, G.A. Plasma End Losses and Heating in the "Low-Pressure", Regime of a Theta Pinch. *Phys. Fluids* **1965**, *8*, 1168–1175. [CrossRef]
5. Silberg, P.Q. Some Efficiency Measurements of the Theta-Pinch. *J. Appl. Phys.* **1966**, *37*, 2155–2161. [CrossRef]
6. Gribble, R.F.; Little, E.M.; Morse, R.L.; Quinn, W.E. Faraday Rotation Measurements on the Scylla IV Theta Pinch. *Phys. Fluids* **1968**, *11*, 1221–1226. [CrossRef]
7. Yarborough, W.W.; Barach, J.P. Current sheet observations in a small theta pinch. *Phys. Fluids* **1975**, *18*, 105–108. [CrossRef]
8. Lee, S. *Radiations in Plasmas*; McNamara, B., Ed.; World Scientific: Singapore, 1984; pp. 978–987.
9. McKenna, K.F.; Siemon, R.E. Theta-pinch research at Los Alamos. *Nucl. Fusion* **1985**, *25*, 1267–1270. [CrossRef]
10. Luna FR, T.; Cavalcantiz, G.H.; Trigueirosy, A.G. A theta-pinch as a spectroscopic light source. *J. Phys. D Appl. Phys.* **1998**, *31*, 866–872. [CrossRef]
11. Awe, T.J.; Siemon, R.E.; Bauer, B.S.; Fuelling, S.; Makhin, V.; Hsu, S.C.; Intrator, T.P. Magnetic Field and Inductance Calculations in Theta-Pinch and Z-Pinch Geometries. *J. Fusion Energy* **2006**, *26*, 17–20. [CrossRef]
12. Lee, S.; Lee, P.; Saw, S.H.; Rawat, R.S. Numerical experiments on plasma focus pinch current limitation. *Plasma Phys. Control. Fusion* **2008**, *50*, 065012. [CrossRef]
13. Cavalcanti, G.H.; Farias, E.E. Analysis of the energetic parameters of a theta pinch. *Rev. Sci. Instrum.* **2009**, *80*, 125109. [CrossRef]
14. Jung, S.; Surla, V.; Gray, T.K.; Andruczyk, D.; Ruzic, D.N. Characterization of a theta-pinch plasma using triple probe diagnostic. *J. Nucl. Mater.* **2011**, *415*, 993–995. [CrossRef]
15. Chaisombata, S.; Ngamrungroj, D.; Tangjitsomboona, P.; Mongkolnavina, R. Determination of Plasma Electron Temperature in a Pulsed Inductively Coupled Plasma (PICP) device. *Procedia Eng.* **2012**, *32*, 929–935. [CrossRef]
16. Lee, S.; Saw, S.H.; Lee PC, K.; Akel, M.; Damideh, V.; Khattak, N.A.D.; Mongkolnavin, R.; Paosawatyanyong, B. A model code for the radiative theta pinch. *Phys. Plasmas* **2014**, *21*, 072501. [CrossRef]
17. Ebrahim, F.A.; Gaber, W.H.; Abdel-Kader, M.E. Estimation of the Current Sheath Dynamics and Magnetic Field for Theta Pinch by Snow Plow Model Simulation. *J. Fusion Energy* **2019**, *38*, 539–547. [CrossRef]
18. Cistakov, K.; Christ, P.; Manganelli, L.; Gavrilin, R.; Khurchiev, A.; Savin, S.; Iberler, M. Study on a dense Theta pinch plasma for ion beam stripping application for FAIR. *J. Recent Contrib. Phys.* **2020**, *75*, 14–21. [CrossRef]
19. Christ, P.; Cistakov, K.; Iberler, M.; Laghchioua, L.; Mann, D.; Rosmej, O.; Savin, S.; Jacoby, J. Measurement of the free electron line density in a spherical theta-pinch plasma target by single wavelength interferometry. *J. Phys. D Appl. Phys.* **2021**, *54*, 285203. [CrossRef]
20. Wang, Z.; Cheng, R.; Wang, G.; Jin, X.; Tang, Y.; Chen, Y.; Zhou, Z.; Shi, L.; Wang, Y.; Lei Yu Wu, X.; et al. Observation of plasma dynamics in a theta pinch by a novel method. *Matter Radiat. Extrem.* **2023**, *8*, 045901. [CrossRef]
21. Djorovic, S.; Pavlov, M. Measurements of specific heats ratio of hydrogen plasmas. *Beiträge Plasmaphys.* **1984**, *24*, 105–112. [CrossRef]
22. Available online: https://www.nt-tao.com/ (accessed on 13 December 2024).
23. Raizer, Y.P. *Gas Discharge Physics*; Springer: Dordrecht, The Netherlands, 1991.
24. Griem, H.R. *Principles of Plasma Spectroscopy*; Cambridge University Press: Cambridge, UK, 1997.
25. Konjević, N.; Ivković, M.; Sakan, N. Hydrogen Balmer lines for low electron number density plasma diagnostics. *Spectrochim. Acta Part B Spectrosc.* **2012**, *76*, 16–26. [CrossRef]

26. Ohno, N.; Razzak, M.A.; Ukai, H.; Takamura, S.; Uesugi, Y. Validity of Electron Temperature Measurement by Using Boltzmann Plot Method in Radio Frequency Inductive Discharge in the Atmospheric Pressure Range. *Plasma Fusion Res.* **2006**, *1*, 28. [CrossRef]

27. Perez, C.; Santamarta, R.; de la Rosa, M.I.; Mar, S. Stark broadening of neutral helium lines and spectroscopic diagnostics. *Eur. Phys. J.* **2003**, *27*, 73–75.

28. Czernichowski, A.; Chapelle, J. Use of 447 nm He I line to determine electron concentration. *J. Quant. Spectrosc. Radiat. Transfer.* **1985**, *33*, 427–435. [CrossRef]

29. Sheffield, J.; Froula, D.; Glenzer, S.H.; Luhmann, N.C., Jr. *Plasma Scattering of Electromagnetic Radiation, Second Edition: Theory and Measurement Techniques*; Academic Press: Cambridge, MA, USA, 2010; ISBN 9780123748775/9780080952031.

30. Miyake, S.; Tsuchida, K.; Uehara, Y.; Sasaki, W.; Watanabe, Y.; Fujita, J. Direct Measurement of Population Inversion in a Recombining Hydrogen Plasma by the La-ser-Induced Fluorescence Method. *Phys. Rev. Lett.* **1983**, *50*, 41–44. [CrossRef]